An Abstract Simulator for Species Concentrations in Channel-Based Microfluidic Devices

Michel Takken *Student Member, IEEE*, Maria Emmerich and
Robert Wille *Senior Member, IEEE*

***Abstract*—The design of microfluidic devices, i.e., *Lab-on-Chips* (LoCs) or *Micro Total Analysis Systems* (µTAS), is a tedious and cumbersome process with many time-consuming and costly fabrication cycles. Many of these devices contain dissolved species (i.e., solutes) that are required to appear in the system at specific pre-defined concentrations. The use of simulations can aid the design process of microfluidic devices. However, methods from *Computational Fluid Dynamics* (CFD), which are commonly used, are computationally costly and require a lot of time to finish. In this work, we present a simulator for species concentrations in channel-based microfluidic devices that operates on a higher level of abstraction and is multiple orders of magnitude faster than CFD simulation methods. The simulator has been implemented in C++ and is benchmarked against CFD simulations as well as against measured results from experiments on a fabricated device. The results are analyzed and the applicability of the simulator for the simulation of microfluidic devices is assessed.**

***Index Terms*—Microfluidic devices, Computational fluid dynamics, Lab-on-a-Chip, Fluid systems, Concentration gradient, Computer simulation**

I. Introduction

In microfluidic devices, or so-called *Lab-on-Chip* (LoC) devices, or *Micro Total Analysis Systems* (µTAS), fluids are manipulated in small volumes, that are considered to be on the micro-scale [1]. Many of them contain dissolved species (i.e., solutes) that should mostly appear in the system at pre-defined concentrations [2]. To assess the performance of these devices, it is important to understand the concentration distribution of these species across the device. For example, in (parts of) some devices, it could be desired that a species is fully mixed (i.e., a homogeneous distribution) [3], e.g., in drug development [4], or clinical diagnosis [5]. For other devices, it could be desired that a specific concentration distribution is acquired, such as in microfluidic cell culture [6, 7], including organs-on-chips [8, 9], cell migration [10], or chemotaxis [11]. No mixture is supposed to occur in devices, such as membraneless microfluidic fuel cells [12, 13]. In any case, all of these devices operate with species suspended in a carrier fluid (continuous phase), and their concentrations strongly influence the performance of these devices. The design of microfluidic devices is a costly and time-consuming process that can be significantly accelerated using simulations to reduce the number of design cycles [14, 15]. Microfluidic devices rely largely on micro-channels with rectangular cross-sections with a width and height of up to a few hundred micrometers [16]. To this end, we are looking for simulation methods that model the concentration distribution of species in channel-based microfluidic devices.

Simulation methods for microfluidic devices can be categorized on different levels of abstraction, i.e., the rate at which the physical world has been abstracted to form a model [17–19]. Methods on a low abstraction level are generally more accurate in their representation of the physical world but are computationally more expensive. Alternatively, high abstraction-level methods can provide simulation results relatively fast but are less accurate [17]. High abstraction simulation methods are generally used to obtain first estimates of the performance of a microfluidic device [14, 15] or are used for cases that are too big to be simulated on a low abstraction level, such as for devices with *microfluidic Very Large Scale Integration* (mVLSI) technology [20, 21].

The general approach for simulating microfluidic devices is to use methods from *Computational Fluid Dynamics* (CFD), that solve governing equations containing partial differentials, such as the Navier-Stokes equations [22–24]. These methods are quite versatile and can simulate a wide range of microfluidic devices, and are considered state-of-the-art [25–28]. However, they require multiple steps to simulate the problem, such as creating a geometry, generating the mesh, and adequately describing the problem. All this requires substantial expertise [27]. Once all that has been covered, there are many computational tools available (both open-source [29, 30] and commercial) to solve the resulting equation system and, hence, simulate the considered system. Even then, another issue remains: These methods are computationally expensive as they scale quadratic (for 2D simulations) or even cubic (for 3D simulations) with the problem's size and complexity, and can take days or even weeks to simulate large problems [31]. These simulation methods are, therefore, only suitable for small, dedicated (parts of) microfluidic devices.

In contrast, abstract simulation methods (based on governing equations for simplified problems, such as the Hagen-Poiseuille Law) are easier to use since no explicit geometry has to be drawn, and no mesh has to be generated [14]. More importantly, these methods are more efficient than CFD methods, and, can even be used to compute the required time to obtain full mixing of species in a microfluidic channel. In fact, currently, abstract simulation approaches for species concentration in microfluidic devices are already used to estimate the required channel lengths to acquire fully mixed mixtures [32] or assume instantaneous mixing at the nodes [33]. This is great for microfluidic devices that require fully mixed mixtures, such as certain chemical and biotechnological assays [4, 5, 34], which sometimes even employ dedicated mixing modules [35]. However, while this

method can produce simulation results in negligible runtime and also for larger microfluidic devices, it is only applicable for devices that are supposed to generate full mixtures. For many microfluidic devices, a full mixture is in fact not desired, but rather some kind of concentration gradient [6–11] or no mixing at all [12, 13]. Hence, on a high abstraction level, a *generalized* simulator for concentration distribution is unfortunately not yet available.

In this work, we aim to close this gap and accelerate the design of microfluidic devices by providing a simulator for species concentrations at a high abstraction level. We propose an abstract simulator for species concentrations in microfluidic devices that is orders of magnitudes faster than CFD methods. To this end, we present a method that

1) constructs the concentration distributions flowing into all channels of a microfluidic device (based on the network topology), and

2) subsequently propagates the respective distributions through all channels using the Advection-Diffusion equation.

By that, we get a simulator that works at a high level of abstraction (and can, hence, efficiently handle larger, more complex devices) while simultaneously generating results comparable to CFD simulations. To verify and validate the proposed method, the resulting simulator was compared against simulations from CFD as well as against measured results obtained from experiments on a fabricated device.

In the following, we describe the employed method and the verification, as well as the validation steps as follows: First, the governing equations for fluid dynamics and species concentrations are reviewed for microfluidic devices in Section II. In Section III, the considered problem and the method are described for a simple mixing channel (illustrating the main idea) before the extension for general channel-based microfluidic devices is described in Section IV. Results obtained from the comparisons against CFD simulations as well as against measured results from experiments performed on a fabricated device are summarized in Section V. These comparisons are then discussed in Section VI. Finally, the paper is concluded in Section VII.

II. Governing Equations

Problems in fluid dynamics are solved using the governing equations for fluids, which, in some cases and depending on the type of problem, can be simplified. The possibility of simplifying the governing equations depends on various factors, one of which is the nature of the fluid problem. More precisely, the nature of a fluid problem is described by a set of so-called dimensionless numbers. In this section, first, the dimensionless numbers for fluids carrying physical species are reviewed, and afterwards, the corresponding governing equations are reviewed. Both provide the basis for the simulation approach presented in this work.

A. Dimensionless Numbers

The dimensionless numbers for fluids carrying species are the Reynold's number and the Peclét number. The Reynold's number is used to describe how organized a flow is; a low Reynold's number means laminar flow, whereas a high number indicates turbulence [22]. It describes the ratio between inertial and viscous forces in a fluid dynamic system, i.e.,

$$Re = \frac{\rho \boldsymbol{u} L}{\mu}, \tag{1}$$

with ρ being the fluid's density, $\boldsymbol{u}$ the fluid velocity, L the characteristic length, and μ the dynamic viscosity of the fluid. For a channel-based microfluidic device, the characteristic length L, is usually set equal to the width of a channel.

Similarly, the nature of the transport of a physical species in a fluid system is described by the Peclét number, which describes the ratio of advective over diffusive transport rate [36], and is given by

$$Pe = \frac{\boldsymbol{u} L}{D}, \tag{2}$$

where D is the diffusivity coefficient of the species carried by the continuous phase in a fluid system. Fluid dynamics on microfluidic devices is usually characterized by its relatively low Reynold's number (i.e., strongly laminar flow) and high Peclét number (i.e., the transport of species is strongly dominated by advection).

B. Hagen-Poiseuille Law

The general governing equations for the flow and pressure fields of a fluid problem are the Navier-Stokes equations [22]. For liquid fluids, at low Reynold's number, the Navier-Stokes equations can be reduced to the Stokes equations [37], which are described by the mass equation

$$\nabla \cdot \boldsymbol{u} = 0, \tag{3}$$

and the momentum equation

$$\mu \nabla^2 \boldsymbol{u} = \nabla p, \tag{4}$$

with p being the pressure of the fluid. If the fluid is considered to flow through a channel, these governing equations can be further reduced to the Hagen-Poiseuille Law, i.e.,

$$\Delta p = Q \cdot R_H. \tag{5}$$

Here, Δp is the pressure difference along a channel, Q is the volumetric flow rate through that channel, and R_H is the hydraulic resistance. The hydraulic resistance is a parameter that depends on the geometry of a channel, e.g., for a 2D rectangular channel, the hydraulic resistance is given by

$$R_H = \frac{w^3 L}{12\mu}, \tag{6}$$

where w and L are the channel width and length, respectively. The similarity between the Hagen-Poiseuille law and Ohm's law for electrical systems is evident, and for complex networks of microfluidic channels, the flow rates and pressures in the network can be calculated using methods analogous to those used for electrical circuits, such as Kirchhoff's laws [38, 39].

C. Advection-Diffusion Equation

The transport of a physical species within a carrier fluid is governed by the Advection-Diffusion equation [40], resulting in a concentration field of the species. The Advection-Diffusion equation in general form is given by

$$D\left(\nabla^2 C\right) = \boldsymbol{u} \cdot \nabla C. \tag{7}$$

Here, C is the concentration. For high Peclét numbers, the transport of species is dominated by advection, as opposed to diffusion. For flow through channels at low Reynold's number, the flow can be assumed to solely flow along the channel and the diffusion in this direction can be neglected [41]. Eq. (7) can be reduced to

$$D\left(\frac{\partial^2 c}{\partial y^2}\right) = u_x \frac{\partial c}{\partial x}, \tag{8}$$

with x being the direction along the channel and y being the lateral direction of a channel. This equation can be rewritten in its dimensionless form [41] as

$$\frac{\delta^2 c^*}{\delta y^{*2}} = Pe \frac{\delta c*}{\delta x*}. \tag{9}$$

Here, the asterisks indicate the dimensionless form of the concentration $c^* = c/c_0$, and $x^* = x/L$, and $y^* = y/w$ are the dimensionless position along the channel and the lateral position, respectively, where c_0 is a reference concentration, L is the channel length, and w is the channel width. Eq. (9) is the governing equation that can be used for the concentration distribution of species within microfluidic channels. How exactly Eq. (9) can be used for a mixing channel is described next.

III. Abstract Simulation of Species Concentrations

The (bio-)chemical species concentrations are fundamental in many microfluidic devices and an adequate simulation of concentrations is, therefore, key. However, depending on the microfluidic device, various rates of mixing can be desired and the considered problem is first reviewed in this section. The versatility of CFD methods allows them to be used to simulate many of these devices, but these methods can easily become computationally expensive. Motivated by this, we propose an alternative solution, which is described using a simple mixing channel as an example. Afterwards, in Section IV, this solution is described in more detail for general microfluidic networks.

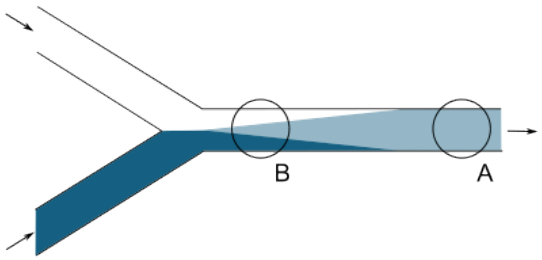

Fig. 1: Schematic concentration distribution in a microfluidic channel.

A. Considered Problem

Mixing in a channel-based microfluidic device occurs once two or more channels filled with a liquid, continuous phase containing different species, or species at different concentrations, merge. E.g., consider the junction with two merging channels, as illustrated in Fig. 1. If a channel is long enough, the two mixing parts will eventually fully mix, as depicted by region A in Fig. 1, and form a new homogeneous mixture. The required channel length to obtain full mixing strongly depends on the flow speed and the diffusivity of the species, and is generally multiple orders of magnitudes larger than the channel width [32]. This means that, for the largest part of a channel, the mixture is not fully mixed and concentration gradients are present, as depicted by region B in Fig. 1. Moreover, microfluidic devices that are not designed for full mixing, generally do not contain channels that are long enough to obtain full mixing and, hence, non-fully mixed mixtures dominate the system. For devices that consider microfluidic cell culture [6–11], a specific concentration gradient is of importance. Some devices even comprise junctions as the example from Fig. 1 with the desire to have the least possible mixing, while fulfilling other performance requirements [12, 13]. For these devices it is important to understand what the concentration gradient along the width at a certain location in the network is, or how long it takes until a tolerated amount of mixing is passed. An abstract simulation method, that can be used to answer these questions, has not yet been exploited and engineers still only have CFD methods available for simulations.

B. Illustration of the Proposed Idea

In this work, we present a simulator that exploits an abstract simulation method to simulate the concentration distribution for general channel-based microfluidic devices. This simulator can be used as an abstract alternative to CFD simulations for microfluidic devices where concentrations play an important role, but fully mixed mixtures do not occur. It uses Eqs. (5) and (6) to calculate the pressure and velocity in a channel as well as Eq. (9) to calculate the concentration distribution at the end of a channel. Based on that, the simulator subsequently propagates that distribution to channels downstream. This idea is illustrated in the following.

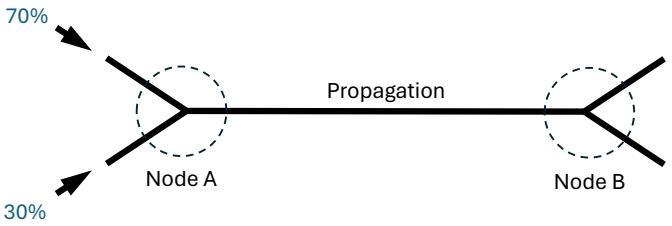

(a) Schematic illustration of a simple mixing channel.

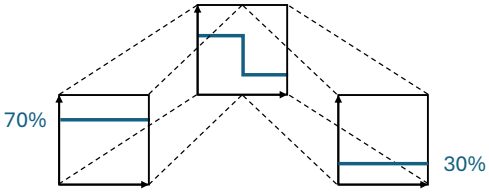

(b) At node A, concentration distributions are merged.

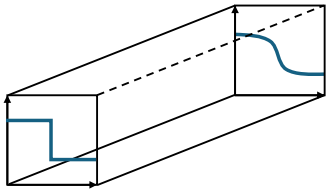

(c) Propagation and diffusion of the concentration distribution in the mixing channel.

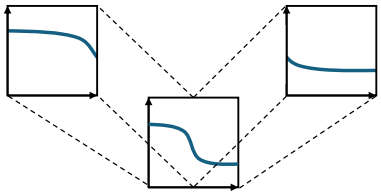

(d) At node B, concentration distribution is split.

Fig. 2: Schematic illustration of propagating the concentration distribution.

To this end, let us consider a simple mixing channel and, by this, illustrate how the concepts of abstract simulation can be employed for simulating the concentration distribution in a channel-based microfluidic device. A schematic illustration of such a simple mixing channel is given in Fig. 2a, where the mixing channel is the channel between Nodes A and B. The channel length is considered to be such that the mixtures are not fully mixed at the end. Without loss of generality, two separate flows with equal flow rates enter the channel at Node A, the bottom one containing a species at a relative concentration of 30% and the top one of 70%. Due to the highly laminar nature of the flow in this system, these two flows are expected to stay organized as they enter the mixing channel at Node A. Fig. 2b illustrates how the two concentration profiles of the incoming flows merge and form the concentration distribution of the flow in the mixing channel, directly at Node A. Subsequently, as the flow progresses, the species is propagated from Node A to Node B at the channel's flow rate, and so is the concentration distribution. During this propagation, the concentration distribution will change due to the diffusion of the species across the channel width, as is illustrated in Fig. 2c. Once the species reaches Node B, the concentration distribution is expected to split according to the respective flow rates of the channels downstream, due to the highly laminar nature of the flow. This is illustrated in Fig. 2d.

With the merge, propagation, and split operations as presented in Fig. 2, we now have the means to conduct an abstract simulation of the concentration distribution for a simple mixing channel. In order to implement the proposed idea in general channel-based microfluidic networks, these operations need to be extended, which is described in more detail in the following section.

IV. Generalization for Microfluidic Networks

We now consider general devices with a network of multiple nodes and channels. To this end, we will have a different set of nodes and a generalized propagation operation. In addition to the nodes for the simple mixing channel (see Fig. 2a), we consider nodes that connect four channels. In this section, we first describe how we combine the merge and split operations in Fig. 2 into various node operations for the new set of nodes. Afterwards, we derive the general propagation operation.

A. Node Operations

The flow in microfluidic channels is of a highly laminar nature, and we use this characteristic to make the assumption that the concentration gradients are preserved during a merge or split operation. That is, in a merge operation, concentration gradients can simply be concatenated and scaled to the new channel width, and in a split operation, the concentration gradient can be cut and its parts scaled to their respective new channel widths.

Operations at nodes that connect more than three channels can be considered as a set of merge and split operations located at one node. These node operations can be defined for any combination of inflowing and outflowing channels, but in the following, we focus on nodes with 3 and 4 connecting channels. This is a realistic representative setting that covers most of the channel-based microfluidic operations that are also considered in, e.g., modular microfluidics [42].

Considering these connections, and the fact that a node will always need one channel for incoming and one for outgoing flow, there are six possible node operations, which are illustrated in Fig. 3. The two 3-way node operations are given in Figs. 3a and 3b and are the same operations as illustrated in Figs. 2b and 2d. The four 4-way node operations are given in Figs. 3c to 3f. Similar to the process described in Section III, these operations provide concentration distributions that can be propagated in outflowing channels.

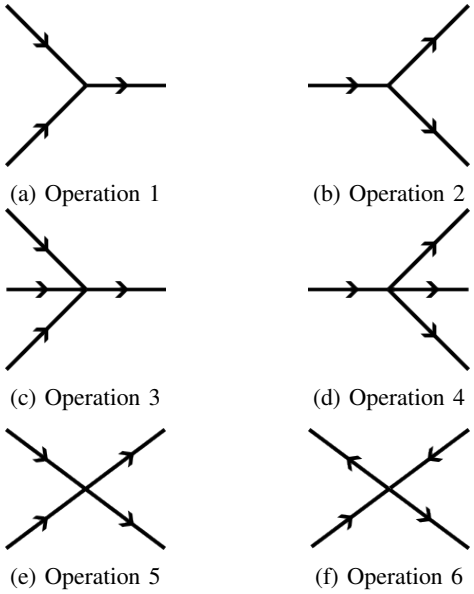

(a) Operation 1 (b) Operation 2

(c) Operation 3 (d) Operation 4

(e) Operation 5 (f) Operation 6

Fig. 3: The 6 operations for mixing in channel-based microfluidic networks, for up to 4 channels at a node.

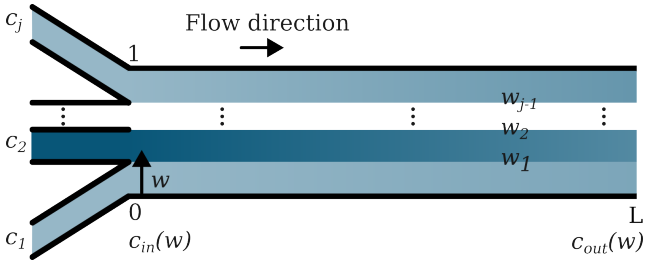

Fig. 4: The incoming constant concentrations $c_1, c_2, ..., c_j$ form the j flow sections that give the concentration distribution $c_{in}(w)$ at the inlet of the channel. The concentration distribution diffuses as it propagates through the channel, resulting in the concentration distribution $c_{out}(w)$ at the end of the channel.

B. Propagation Operation

The concentration distribution throughout the network is governed by the Advection-Diffusion equation reviewed in Section II. In particular, we consider the dimensionless Advection-Diffusion equation for channel flow as given in Eq. (9). We get the solution, for the respective channel outflow, of the concentration distribution across the channel width $c_{out}(w)$, by employing separation of variables and the exponential form of the *Cosine Fourier Series*. Additionally, we apply the Neumann boundary conditions

$$\left.\frac{\partial c}{\partial y}\right|_{x=0} = 0 \quad \text{and} \quad \left.\frac{\partial c}{\partial y}\right|_{x=1} = 0$$

at the channel walls for a channel with a normalized width w from 0 to 1, and the initial condition $c_{in}(w)$, which defines the concentration distribution at the channel inflow. For a set of inflows with constant concentrations, $c_{in}(w)$ is given by

$$c_{in}(w) = \begin{cases} c_1 & 0 \leq w < w_1 \\ c_2 & w_1 \leq w < w_2 \\ \vdots & \vdots \\ c_j & w_{j-1} \leq w \leq 1 \end{cases},$$

where j is the number of flow sections in the channel, resulting from incoming constant concentrations. This is illustrated in Fig. 4, which depicts j flow sections in the channel, resulting from the incoming constant concentrations. The sum of concentration inflows then describe $c_{in}(w)$ and we define the bounds of w (i.e., $0, w_1, w_2, ..., w_{j-1}, 1$ in Fig. 4) for the respective flow section as a and b. This results in the concentration profile at the channel end defined by

$$c_{out}(w) = \frac{a_0}{2} + \sum_{n=1}^{\infty} a_n \cdot cos(n\pi w) \cdot exp\left(\frac{-n^2\pi^2}{Pe} L\right), \quad (10)$$

with

$$a_n = 2 \int_a^b c_{in}(w) \cdot cos(n\pi w)\, dw\,, \quad n \in \mathbb{N}_0, \quad (11)$$

where L is the channel length. We normalize the channel width to 1 for all channels, and define multiple flow sections in one channel, using the bounds. Eqs. (10) and (11) form the analytical solution to Eq. (9), for the given boundary conditions and initial condition.

As soon as one or more of the concentration inflows are non-constant, we need to define its (now inflow) profile based on Eq. (10). Here, we consider four aspects:

1) The initial concentration inflow, e.g. at the pumps, needs to be constant. More precisely, all concentration definitions at the start of the microfluidic channel network that are defined for this simulation approach need to have a constant value or be approximated as a combination of several constant values. Conveniently, this aligns with most experimental set-ups.

2) The infinite sum in Eq. (10) needs to be truncated, to be able to efficiently run the simulation. This is achieved by defining a finite, case-dependent limit, where the effect of further addends on the result is negligible. In general, truncating the sum at $n \approx 100$ is sufficient.

3) The concentration needs to be propagated through the network. This is done by defining (sections of) the ouflow distribution(s) $c_{\text{out}}(w)$ of the previous channel(s) as the inflow distribution $c_{\text{in}}(w)$ in Eq. (11). By employing trigonometric identities, we can continue to integrate Eq. (11) and calculate the outflow distribution $c_{\text{out}}(w)$ of the considered channel.[1] These steps can be applied recursively to obtain the concentration profiles throughout a channel-based microfluidic network.

[1]Details of the mathematical expressions are available in the supplementary material.

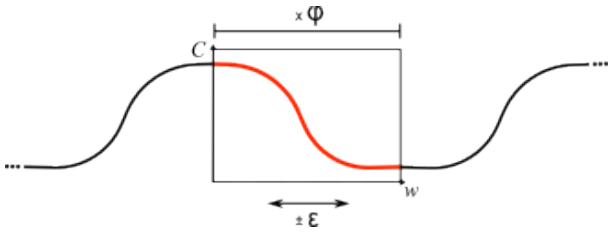

Fig. 5: An incoming concentration distribution that is non-constant needs to be scaled and translated to fit the flow section in the channel it flows into. The scale factor φ and translate factor ε affect the concentration profile $c(w)$.

4) During propagation of a non-constant concentration channel inflow, we need to consider the effect of channels splitting and merging. The principle is explained in Section IV-A. In short, changes in volumetric flow rate when channels merge or split impact the bulk fluid flow section and, subsequently, the concentration distribution across the channel width. In Fig. 5, an exemplary concentration profile is depicted. The section of the graph, highlighted in red, represents the concentration profile across the channel width, represented by the square. Changes of the channel width, or the bulk fluid flow section, including merging or splitting are implemented by adapting the function graph by employing two mathematical operations:

   - We scale the function $c_{in}(w)$ using a scale factor
   $$\varphi = \frac{b-a}{d-c}, \tag{12}$$
   where c and d are the bounds of the flow section coming from the previous channel. By this, the concentration profile along the x-axis, i.e. the channel width, is scaled.
   - We move the function along the x-axis using a translate factor
   $$\varepsilon = \frac{a}{\varphi} - c \tag{13}$$
   to make sure the desired section of the function is considered.

   This results in an adapted input concentration $c_{in}(\varphi w - \varepsilon)$. Consider the example of a splitting channel in Fig. 2d, the channel split impacts the concentration profile. To look at the correct channel sections for the subsequent channels, we scale the graph to twice its extent, and for one of the channels, we translate the observed section to the side. Otherwise, we would consider the same section twice.

Overall, this generalizes the idea proposed in Section III and yields a solution that is applicable to microfluidic devices with up to four channels per node. This solution allows the calculation of the diffusion-based concentration profile in microfluidic networks at defined channel lengths and works both for constant concentration inflow as well as the propagation of generated concentration profiles, including channel merging, splitting, and scaling. More generalized equations and test cases are defined in the open-source implementation (see next section). In the following, the resulting concentration distributions are compared and validated using CFD, and experimental results.

V. Evaluation and Validation

The method described in Section IV has been implemented in C++ as an abstract species concentration simulator and it is available in open source as part of the *Munich Microfluidics Toolkit* (MMFT) [43]. In this section, we evaluate and validate the developed simulator on a set of benchmarks. To this end, we used OpenFOAM [29] to generate the CFD baseline. Besides that, we simulated a device fabricated by Jeon et al. [32] and compared the results to measurements obtained from physical experiments [32]. In this section, first, the test cases that were used as benchmarks are presented. Afterwards, the obtained results from the simulator are compared against results obtained from CFD simulation. Finally, we present the simulated and measured concentration profiles for the fabricated device.

A. Test Cases

To benchmark the simulator, it was required to test it for various combinations of node operations (i.e., different networks), with dimensions that are representative of microfluidic devices, and for a wide range of relevant Peclét numbers. To this end, we used four microfluidic networks, that are used for the test cases, which are illustrated in Fig. 6 and are described in more detail below.

- Case 1: The geometry of this case is shown in Fig. 6a. This case is the simple mixing channel from Fig. 2. The channel widths are 100 µm.
- Case 2: The geometry of this case is similar to that of Case 1, except that it has an additional set of inflow and outflow channels, as depicted in Fig. 6b. This case consists of Node Operations 3 and 4 (see Figs. 3c and 3d). Two channels were given a width of 200 µm and the others were given a width of 100 µm.
- Case 3: The third case is a sequence of Node Operation 5 (see Fig. 3e) with a collection of channels with a width of 100 µm, and with an increased width of 200 µm, as illustrated in Fig. 6c.
- Case 4: The final case combines a set of Node Operation 1, 3, and 6 (see Figs. 3a, 3c and 3f). It is illustrated in Fig. 6d. All channel widths are 100 µm.

All test cases have been simulated using both CFD simulation and the proposed abstract approach. To benchmark the abstract simulator for different geometries (and, hence, node operations), the test cases were conducted at similar Peclét numbers for the four geometries. To this end, the diffusion coefficient D of the species was always set to 10^{-8} m^2/s, all inlet flow velocities were set to 10 mm/s, and the channel widths (with exception of some, to test the simulator's performance for varying channel width) were generally set at 100 µm.

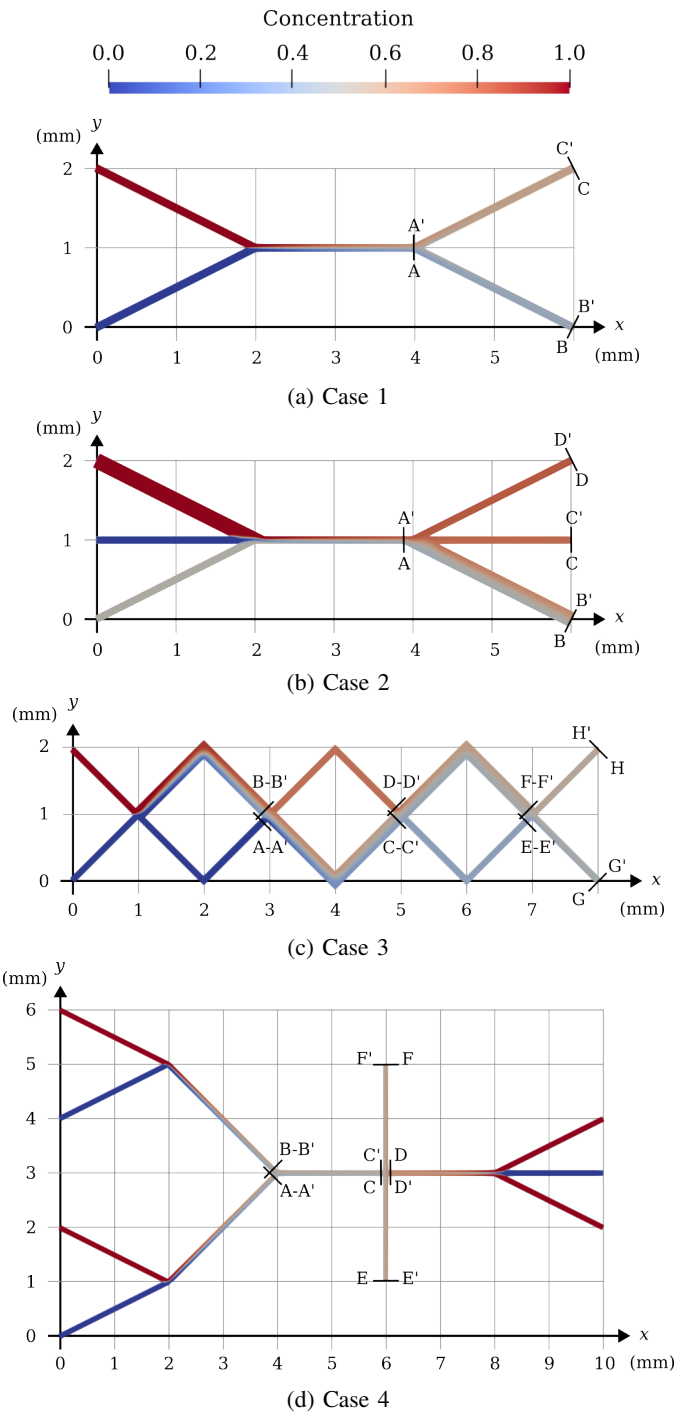

(a) Case 1

(b) Case 2

(c) Case 3

(d) Case 4

Fig. 6: Geometries of the four test cases and the corresponding CFD results for the concentration field C. The coordinates are given in millimeters.

Additionally, to test the simulator's performance for a wide range of Peclét numbers, we conducted different simulations using the geometry of Case 1 (see Fig. 6a), with variable mixing channel length cL. The diffusivity coefficient and inlet flow velocity were changed such that the test cases would cover a range of Peclét numbers from 100 to 10,000 for mixing channel lengths of 2, 10, and 20 mm. Overall, this resulted in 60 simulation instances that have been considered. The results

TABLE I: The runtimes of the cases illustrated in Fig. 6 as simulated using CFD and the proposed abstract method given in seconds together with the corresponding speed-up

	Runtimes		
Case	CFD [s]	Abstract [s]	Speed-up
1	1208.9	< 0.01	$\geq \mathcal{O}(10^5)$
2	2301.6	< 0.01	$\geq \mathcal{O}(10^5)$
3	2521.9	0.02	$\mathcal{O}(10^5)$
4	1600.7	0.01	$\mathcal{O}(10^5)$

of the abstract and CFD simulator of all of these test cases are presented next.

B. Comparison against CFD Simulations

To generate the CFD baseline, against which the results from the abstract simulator can be tested, OpenFOAM [29] was used. The resulting concentration fields of the CFD simulations are visualized in Fig. 6. The runtimes of the CFD simulations and the proposed abstract simulations are given in Table I, together with the corresponding speed-up for each case. The abstract and CFD results were compared for all test cases and the concentration distribution was taken at pre-defined cross-sections, denoted in Fig. 6 as A-A'...G-G'. The resulting concentration distributions for all cross-sections are given in Fig. 7, where the concentration values are here given as a percentage of the maximal concentration present in the corresponding test case.

Besides that, Case 1 was simulated for different sets of diffusion coefficients, inlet velocities (hence, Peclét numbers), and mixing channel lengths. The mean squared errors for these various cases are given in Fig. 8, showcasing the robustness of the method at a large range of Peclét numbers. As a reference, the case illustrated in Fig. 7a has a Peclét number of 100 and a mixing channel length of 2 mm.

In general, the concentration distributions of the abstract simulator are well in line with the CFD simulation results. The results of the abstract simulator were obtained in negligible runtime, which is significantly less than the CFD simulations, which took about 20 to 40 minutes to generate the flow field and concentration distribution, resulting in a notable speed-up of $\mathcal{O}(10^5)$ for all cases.

C. Comparison against Measured Results

Since CFD results do not necessarily provide the ground truth, the simulator was also compared against measured results from experiments performed on a fabricated device, as reported by Jeon et al. [32]. The gradient generator described by Jeon et al. has three inlets, six layers of mixing channels, and nine channels coming together into a single outlet, as illustrated in Fig. 9. Jeon et al. measured the concentration distribution 500 µm downstream in the outlet channel for inlet channel velocities of 1 mm/s, 10 mm/s, and 100 mm/s, respectively. For these three experiments, the inlet concentrations were kept constant at 100% for the middle inlet, and 0% for the left and

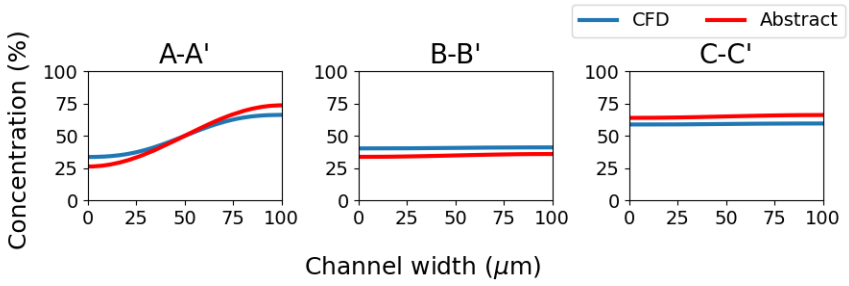

(a) Case 1

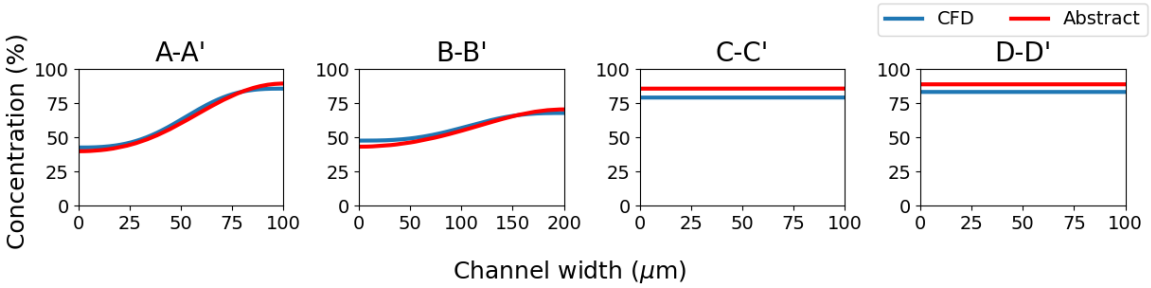

(b) Case 2

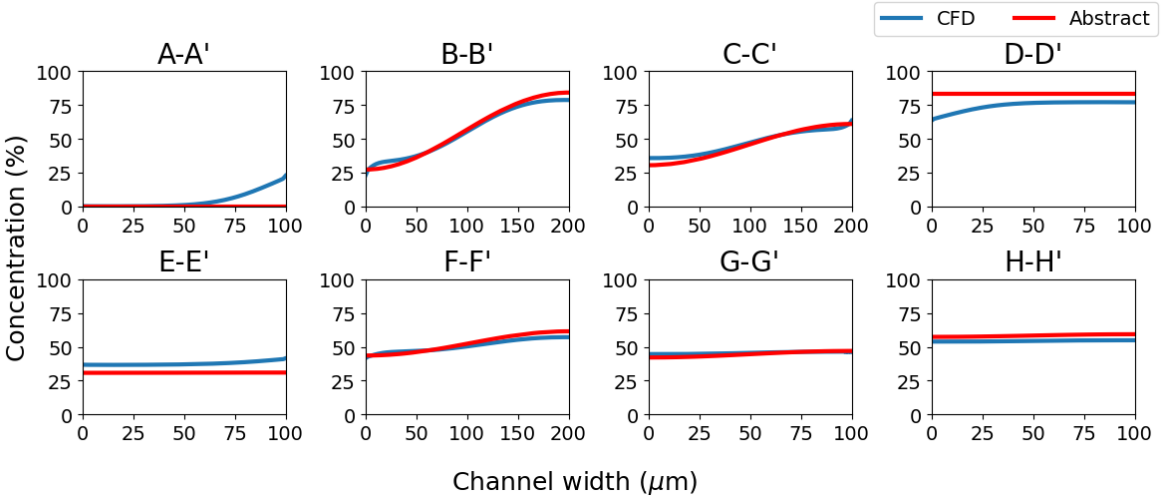

(c) Case 3

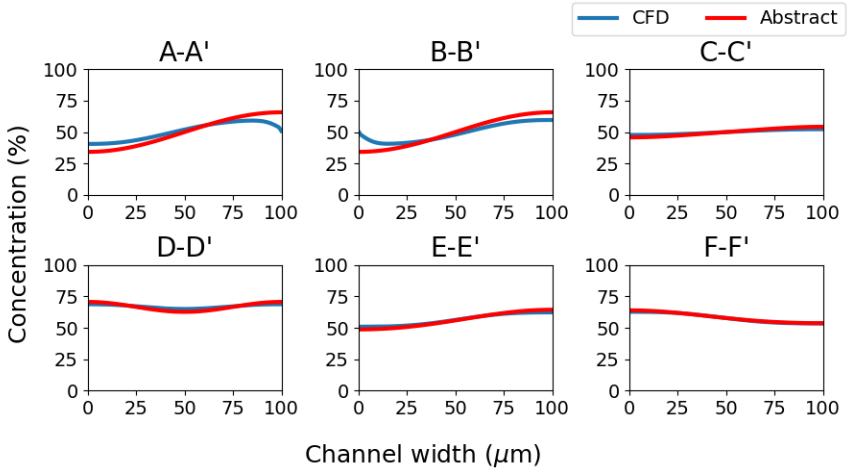

(d) Case 4

Fig. 7: Graphs of Abstract and CFD concentration distributions.

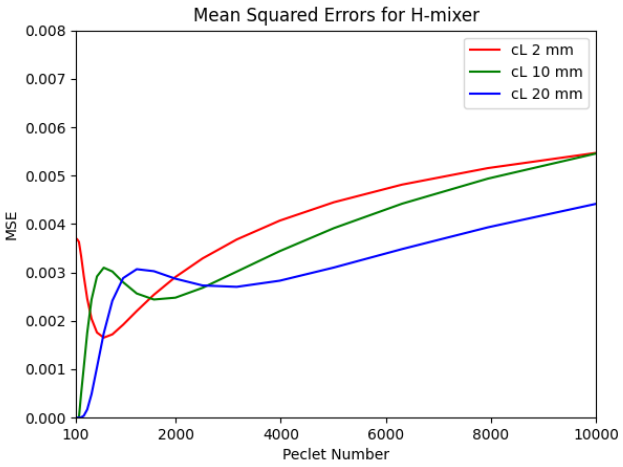

Fig. 8: The mean squared error between the abstract and CFD simulators for test-case 1 at different Peclét numbers and channel lengths.

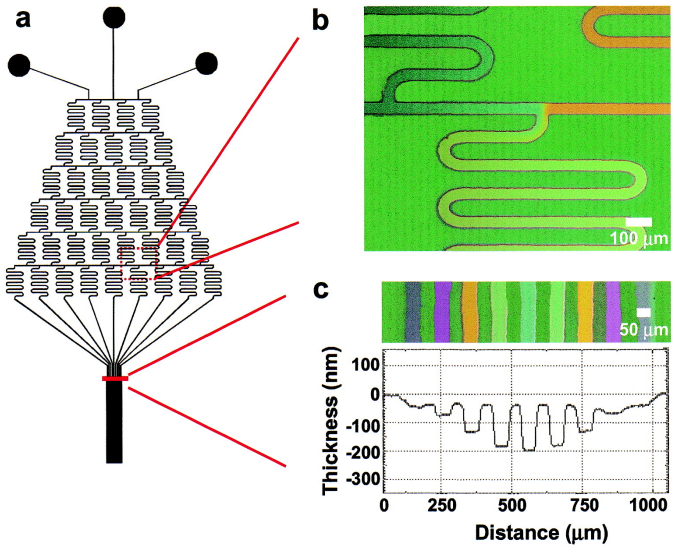

Fig. 9: The geometric setup used for obtaining experimental data, with (a) the complete geometry of meandering channels with three inlets and nine channels coming together to form the outlet, (b) a detailed depiction with scale of the connecting channels, and (c) the depth of the nine channels coming together at the outlet. Reprinted with permission from Jeon et al. [32] Copyright 2024 American Chemical Society.

right inlets. The Peclét numbers of these three experiments are 100, 1,000, and 10,000, respectively.

The concentration distributions obtained from the simulations were compared against those measured in the experiment. This comparison is summarized in Fig. 10, which shows that the simulation results align well with experimental results for the three cases. It should be noted that flows in the cases with 1 and 10 mm/s inlet velocity are slow enough to obtain fully mixed mixtures in the meandering channels, whereas the flow in the case with 100 mm/s inlet velocity is too fast to obtain full mixing in the meandering channels. Whether mixtures were fully mixed or not did not have a significant effect on the accuracy of the simulator, additionally showcasing its general applicability.

VI. Discussion

The results and comparisons given in Section V show that the results obtained by the abstract method are well in line with those obtained from CFD methods and with measurements obtained from experiments performed on a fabricated device. This is particularly impressive considering that all results from the abstract simulator have been generated in negligible runtime (see Table I). This makes the proposed approach a suitable alternative for simulating species concentrations in large-scale channel-based microfluidic devices, or mVLSI devices, for which CFD simulators are too expensive and an alternative is needed [14, 21].

However, at cross-section A-A' in Fig. 7a, the abstract simulator technically provides the analytical solution to Eq. (9), which is well-known [41] and, thus, a better fit with the CFD results would be expected. This discrepancy is remarkable and some further elaboration on this observation is required. In this section, we will discuss this observed discrepancy. To this end, this discussion is divided into the three operations that are considered in Fig. 6a: The merge operation, the propagation operation, and the split operation. Finally, the applicability of the simulator is discussed.

A. Merge Operation

Firstly, we look at the merge operator and zoom into the merge region of Case 1 (see Fig. 6a), as illustrated in Fig. 11a. At the cross-section M-M', where the incoming flows meet, it is assumed that the concentration distribution would be a simple step-function, as illustrated in Fig. 11b. However, the observed concentration distribution in Fig. 11b shows a slightly smoothed version of the step function. Here, it should be noted that the *Finite Volume Method* (FVM) [23], which is the core method of OpenFOAM [29], is a fundamentally diffusive method, meaning that the observation could also be an effect of, or amplified by, numerical diffusion [31]. However, it is more likely that this discrepancy is caused by a relatively high diffusion coefficient, resulting in the relatively low Peclét number of 100. Even though diffusive mixing is slow compared to the lateral velocity of the flow, the test case is still at a Peclét number that is low enough, for diffusion to play a noticeable role. This is also observed for, e.g., cross-sections A-A' and B-B' of Case 4 (see Fig. 7d). This discrepancy dominates the MSE for relatively low Peclét numbers as can be seen in the graphs in Fig. 8, which show peaks in the low Peclét number region for all channel lengths.

B. Propagation Operation

Secondly, due to the abstraction of the geometry, the computed mixing length (and, hence, time) is slightly shorter than the effective mixing length. This is illustrated in Fig. 12, where the real geometry is shown in black and its abstracted

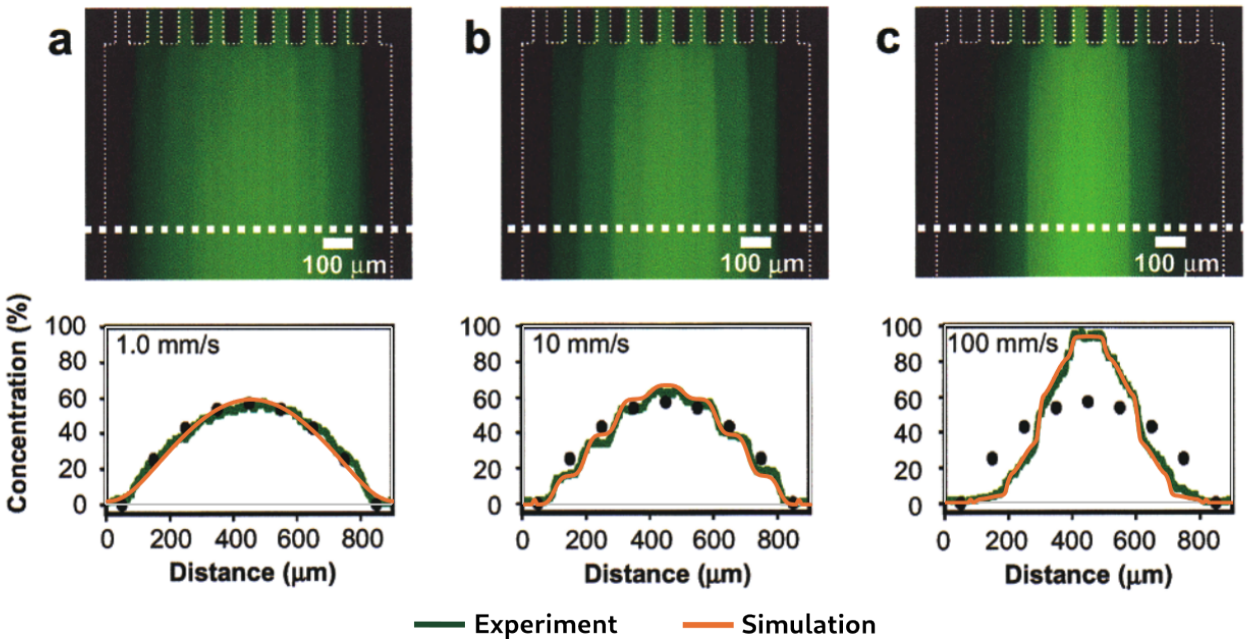

Fig. 10: Comparison of experimental, in dark green, and simulation data, in orange, taken at the white dotted measurement line for inlet flow velocities of (a) 1 mm/s, (b) 10 mm/s, and (c) 100 mm/s. The comparison is done 500 µm downstream in the outlet channel. Adapted with permission from Jeon et al. [32] Copyright 2024 American Chemical Society.

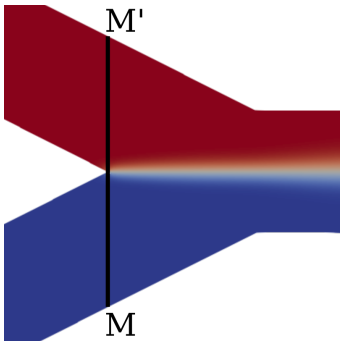

(a) Zoomed in merge-region with cross-section M-M'.

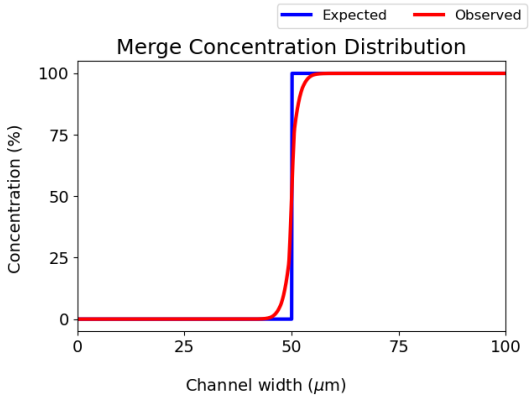

(b) Expected (in blue) and observed (in red) concentration distributions at cross-section M-M'.

Fig. 11: The concentration distribution at the merge operation.

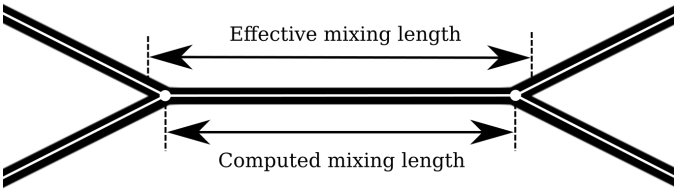

Fig. 12: Schematic representation of the abstraction of a simple mixing channel.

representation in white, as a set of channels and nodes. Here, it becomes obvious that the computed mixing length is shorter due to the abstraction of the merge and split regions into nodes. This effect decreases and eventually disappears for networks with *channel length* $\gg$ *channel width*, as can be seen in the graphs in Fig. 8, where the MSE is lower for cases that have a longer channel. In Case 1 in Fig. 6a, the difference is 11% of the computed mixing length, meaning that a large part of the discrepancy for cross-section A-A' in Case 1 is most likely caused by this.

C. Split Operation

The two effects discussed so far largely disappear at increased Peclét numbers and long mixing channels. At high Peclét numbers, another discrepancy appears for the split operation. Namely, if the concentration distribution is split at a location with a high concentration gradient, localized additional diffusion takes place near the splitting region, as illustrated in Fig. 13a. This localised diffusion is even more clearly visible in Fig. 13b, which shows the concentration distribution

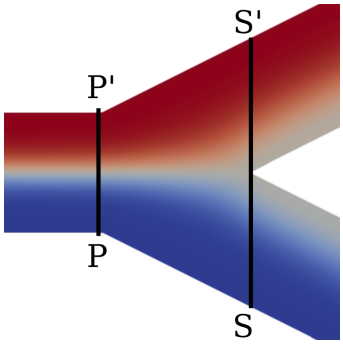

(a) Zoomed in split-region with cross-sections P-P' (before the split) and S-S' (at the split).

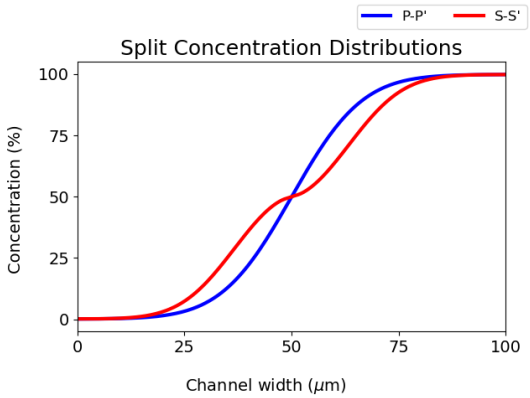

(b) The concentration distributions before the split P-P' (in blue), and directly at the split S-S' (in red).

Fig. 13: The concentration distributions before and at the split operation.

before the splitting region and directly at the split. Additional diffusion occurs in the middle of the channel, which becomes stronger for higher concentration gradients at the middle of the channel.

D. Applicability

Overall, given that the method is an abstract simulation, that provides fast simulation results, the results are well in line, and the discrepancies are less visible for Cases 2-4. Besides that, we subjected the abstract simulator to measurements from experiments on a fabricated device, and the results are well in line as well. From this, we can say that, even though some discrepancies may appear, the simulator performs well for concentration distributions in general channel-based microfluidic devices. For engineers designing corresponding devices, the proposed approach constitutes an efficient means to quickly validate designs in negligible time compared to the efforts of setting up a (computationally expensive) CFD simulation or even fabrication. In particular, for initial design, design space exploration, optimization, and quick prototyping, this provides a powerful solution. The proposed method can be extended for devices that use non-Newtonian flows, given that the viscoelastic instability is not significant and the flow behaves sufficiently laminar [44]. Besides that, the method can be extended for applications that consider an increase or decrease of species concentrations at the wall, originating from, e.g., chemical reactions or diffusion across a membrane. These possible extensions should be researched in future work.

VII. Conclusion

In this work, we presented an approach that simulates the concentration distribution for channel-based microfluidic networks in a *push-button* fashion on an abstract level. Abstract simulation methods for microfluidic devices are necessary to develop large-scale channel-based microfluidic, or mVLSI, devices, for which CFD simulations are too expensive. The simulator uses a method that constructs the concentration distribution flowing into a channel, based on the network topology. The concentration distribution is subsequently propagated through that channel for which the analytical solution of the Advection-Diffusion equation is used. This method was implemented in C++ and benchmarked on a set of test cases, where results obtained from CFD simulations formed the baseline. Additionally, the simulator was compared against measurements obtained from experiments performed on a fabricated device. For the comparison against CFD simulations, some discrepancies were observed. However, given that the simulator's execution time was multiple orders of magnitudes faster than CFD simulations, and given that the obtained results were well in line with most test cases and with the measured concentration distribution of the fabricated device, it can be concluded that the simulator performs well on an abstract simulation level. The presented simulator can be used for general channel-based microfluidic devices and is available in open source as part of the MMFT [43].

Acknowledgements

This work has partially been supported by the FFG project AUTOMATE (project number: 890068) as well as by BMK, BMDW, and the State of Upper Austria in the frame of the COMET Programme managed by FFG.

References

[1] G. M. Whitesides, "The origins and the future of microfluidics," *nature*, vol. 442, no. 7101, pp. 368–373, 2006.

[2] T. M. Squires and S. R. Quake, "Microfluidics: Fluid physics at the nanoliter scale," *Reviews of modern physics*, vol. 77, no. 3, pp. 977–1026, 2005.

[3] C.-Y. Lee and L.-M. Fu, "Recent advances and applications of micromixers," *Sensors and Actuators B: Chemical*, vol. 259, pp. 677–702, 2018.

[4] J. S. Lee, P. Han, R. Chaudhury, S. Khan, S. Bickerton *et al.*, "Metabolic and immunomodulatory control of type 1 diabetes via orally delivered bile-acid-polymer nanocarriers of insulin or rapamycin," *Nature Biomedical Engineering*, vol. 5, no. 9, pp. 983–997, 2021.

[5] P. Yager, T. Edwards, E. Fu, K. Helton, K. Nelson *et al.*, "Microfluidic diagnostic technologies for global public health," *Nature*, vol. 442, no. 7101, pp. 412–418, 2006.

[6] E. W. K. Young and D. J. Beebe, "Fundamentals of microfluidic cell culture in controlled microenvironments," *Chemical Society Reviews*, vol. 39, no. 3, p. 1036, 2010.

[7] A. Yahyazadeh Shourabi, N. Kashaninejad, and M. S. Saidi, "An integrated microfluidic concentration gradient generator for mechanical stimulation and drug delivery," *Journal of Science: Advanced Materials and Devices*, vol. 6, no. 2, pp. 280–290, Jun. 2021.

[8] K. Ronaldson-Bouchard, D. Teles, K. Yeager, D. N. Tavakol, Y. Zhao *et al.*, "A multi-organ chip with matured tissue niches linked by vascular flow," *Nature Biomedical Engineering*, vol. 6, no. 4, pp. 351–371, Apr. 2022.

[9] C. M. Leung, P. de Haan, K. Ronaldson-Bouchard, G.-A. Kim, J. Ko *et al.*, "A guide to the organ-on-a-chip," *Nature Reviews Methods Primers*, vol. 2, no. 1, p. 33, May 2022.

[10] V. V. Abhyankar, M. W. Toepke, C. L. Cortesio, M. A. Lokuta, A. Huttenlocher *et al.*, "A platform for assessing chemotactic migration within a spatiotemporally defined 3D microenvironment," *Lab on a Chip*, vol. 8, no. 9, p. 1507, 2008.

[11] W. Zhao, H. Zhao, M. Li, and C. Huang, "Microfluidic devices for neutrophil chemotaxis studies," *Journal of Translational Medicine*, vol. 18, no. 1, p. 168, Dec. 2020.

[12] Y. Wang, S. Luo, H. Y. Kwok, W. Pan, Y. Zhang *et al.*, "Microfluidic fuel cells with different types of fuels: A prospective review," *Renewable and sustainable energy reviews*, vol. 141, p. 110806, 2021.

[13] N. Khodaparastasgarabad, J. M. Sonawane, H. Baghernavehsi, L. Gong, L. Liu *et al.*, "Microfluidic membraneless microbial fuel cells: new protocols for record power densities," *Lab on a Chip*, vol. 23, no. 19, pp. 4201–4212, 2023.

[14] A. Grimmer, X. Chen, M. Hamidović, W. Haselmayr, C. L. Ren *et al.*, "Simulation before fabrication: A case study on the utilization of simulators for the design of droplet microfluidic networks," *RSC advances*, vol. 8, no. 60, pp. 34 733–34 742, 2018.

[15] G. Fink, F. Costamoling, and R. Wille, "Mmft droplet simulator: Efficient simulation of droplet-based microfluidic devices," *Software Impacts*, vol. 14, p. 100440, 2022.

[16] A.-G. Niculescu, C. Chircov, A. C. Bîrcă, and A. M. Grumezescu, "Fabrication and applications of microfluidic devices: A review," *International Journal of Molecular Sciences*, vol. 22, no. 4, p. 2011, 2021.

[17] M. Takken and R. Wille, "Simulation of pressure-driven and channel-based microfluidics on different abstract levels: A case study," *Sensors*, vol. 22, no. 14, p. 5392, 2022.

[18] G. Fink, P. Ebner, M. Hamidović, W. Haselmayr, and R. Wille, "Accurate and efficient simulation of microfluidic networks," in *Proceedings of the 26th Asia and South Pacific Design Automation Conference*, 2021, pp. 85–90.

[19] M. Takken and R. Wille, "Accelerated computational fluid dynamics simulations of microfluidic devices by exploiting higher levels of abstraction," *Micromachines*, vol. 15, no. 1, p. 129, 2024.

[20] I. E. Araci and S. R. Quake, "Microfluidic very large scale integration (mVLSI) with integrated micromechanical valves," *Lab on a Chip*, vol. 12, no. 16, pp. 2803–2806, 2012.

[21] K. Hu, K. Chakrabarty, and T.-Y. Ho, *Computer-aided design of microfluidic very large scale integration (mVLSI) biochips*. Springer, 2017.

[22] G. K. Batchelor, *An introduction to fluid dynamics*. Cambridge university press, 1967.

[23] J. H. Ferziger, M. Perić, and R. L. Street, *Computational methods for fluid dynamics*. Springer, 2019.

[24] T. Krüger, H. Kusumaatmaja, A. Kuzmin, O. Shardt, G. Silva *et al.*, "The lattice Boltzmann method," *Springer International Publishing*, vol. 10, no. 978-3, pp. 4–15, 2017.

[25] Y. Amini, V. Ghazanfari, M. Heydari, M. M. Shadman, A. G. Khamseh *et al.*, "Computational fluid dynamics simulation of two-phase flow patterns in a serpentine microfluidic device," *Scientific Reports*, vol. 13, no. 1, p. 9483, 2023.

[26] I. Chaves, L. Duarte, W. Coltro, and D. Santos, "Droplet length and generation rate investigation inside microfluidic devices by means of CFD simulations and experiments," *Chemical Engineering Research and Design*, vol. 161, pp. 260–270, 2020.

[27] P. Ebner and R. Wille, "CFD for microfluidics: A workflow for setting up the simulation of microfluidic devices," in *Proceedings of the Euromicro Conference on Digital System Design (DSD), Durres, Albania*, 2023, pp. 6–8.

[28] J. Wang, P. Brisk, and W. H. Grover, "Random design of microfluidics," *Lab on a Chip*, vol. 16, no. 21, pp. 4212–4219, 2016.

[29] H. G. Weller, G. Tabor, H. Jasak, and C. Fureby, "A tensorial approach to computational continuum mechanics using object-oriented techniques," *Computers in physics*, vol. 12, no. 6, pp. 620–631, 1998.

[30] M. Krause, A. Kummerländer, S. Avis, H. Kusumaatmaja, D. Dapelo *et al.*, "OpenLB–Open source lattice Boltzmann code," vol. 81, pp. 258–288, 2021.

[31] T. Glatzel, C. Litterst, C. Cupelli, T. Lindemann, C. Moosmann *et al.*, "Computational fluid dynamics (CFD) software tools for microfluidic applications–a case study," *Computers & Fluids*, vol. 37, no. 3, pp. 218–235, 2008.

[32] N. L. Jeon, S. K. Dertinger, D. T. Chiu, I. S. Choi, A. D. Stroock *et al.*, "Generation of solution and surface gradients using microfluidic systems," *Langmuir*, vol. 16, no. 22, pp. 8311–8316, 2000.

[33] M. Emmerich, F. Costamoling, and R. Wille, "Modular and extendable 1D-simulation for microfluidic devices," *Scientific Reports*, vol. 14, no. 1, p. 26311, 2024.

[34] S. J. Lee and S. Y. Lee, "Micro total analysis system (μ-TAS) in biotechnology," *Applied Microbiology and Biotechnology*, vol. 64, no. 3, pp. 289–299, Apr. 2004.

[35] C.-Y. Lee, C.-L. Chang, Y.-N. Wang, and L.-M. Fu, "Microfluidic mixing: A review," *International Journal of Molecular Sciences*, vol. 12, no. 5, pp. 3263–3287, May 2011.

[36] S. Patankar, *Numerical heat transfer and fluid flow*. CRC press, 2018.

[37] B. J. Kirby, *Micro-and nanoscale fluid mechanics: transport in microfluidic devices*. Cambridge university press, 2010.

[38] K. W. Oh, K. Lee, B. Ahn, and E. P. Furlani, "Design of pressure-driven microfluidic networks using electric circuit analogy," *Lab on a Chip*, vol. 12, no. 3, pp. 515–545, 2012.

[39] A. Grimmer, M. Hamidović, W. Haselmayr, and R. Wille, "Advanced simulation of droplet microfluidics," *ACM Journal on Emerging Technologies in Computing Systems (JETC)*, vol. 15, no. 3, pp. 1–16, 2019.

[40] R. F. Probstein, *Physicochemical hydrodynamics: an introduction*. John Wiley & Sons, 2005.

[41] Z. Wu, N.-T. Nguyen, and X. Huang, "Nonlinear diffusive mixing in microchannels: theory and experiments," *Journal of Micromechanics and Microengineering*, vol. 14, no. 4, p. 604, 2004.

[42] M. Rhee and M. A. Burns, "Microfluidic assembly blocks," *Lab on a Chip*, vol. 8, no. 8, pp. 1365–1373, 2008.

[43] "Munich Microfluidics Toolkit," https://www.cda.cit.tum.de/research/microfluidics/munich-microfluidics-toolkit/, accessed: 2024-06-19.

[44] S. O. Hong, K.-S. Park, D.-Y. Kim, S. S. Lee, C.-S. Lee *et al.*, "Gear-shaped micromixer for synthesis of silica particles utilizing inertio-elastic flow instability," *Lab on a Chip*, vol. 21, no. 3, pp. 513–520, 2021.

Michel Takken received his Master's degree in Computational Science and Engineering from the Technical University of Munich, Germany, in 2021. Currently, he is a Ph.D. student at the Technical University of Munich. His main research interests are simulation for microfluidics devices and fuel cells.

Maria Emmerich received her Master's degree in biotechnology from the Technical University of Berlin, Germany, in 2022. Currently, she is a Ph.D. student at the Technical University of Munich. Her main research interests are design automation and simulation for microfluidics and organs-on-chips.

Robert Wille (M'06–SM'15) is a Full and Distinguished Professor at the Technical University of Munich, Germany, and Chief Scientific Officer at the Software Competence Center Hagenberg, Austria. He received the Diploma and Dr.-Ing. degrees in Computer Science from the University of Bremen, Germany, in 2006 and 2009, respectively. Since then, he worked at the University of Bremen, the German Research Center for Artificial Intelligence (DFKI), the University of Applied Science of Bremen, the University of Potsdam, and the Technical University Dresden. From 2015 until 2022, he was Full Professor at the Johannes Kepler University Linz, Austria, until he moved to Munich. His research interests are in the design of circuits and systems for both conventional and emerging technologies. In these areas, he published more than 400 papers and served in editorial boards as well as program committees of numerous journals/conferences such as TCAD, ASP-DAC, DAC, DATE, and ICCAD. For his research, he was awarded, e.g., with Best Paper Awards, e.g., at TCAD and ICCAD, an ERC Consolidator Grant, a Distinguished and a Lighthouse Professor appointment, a Google Research Award, and more.